



<b>Publication Year</b>	2019
<b>Acceptance in OA @INAF</b>	2021-02-18T16:02:41Z
<b>Title</b>	Spectral Energy Distribution of Blue Stragglers in the Core of 47 Tucanae
<b>Authors</b>	RASO, SILVIA; PALLANCA, CRISTINA; Ferraro, Francesco R.; Lanzoni, Barbara; Mucciarelli, Alessio; et al.
<b>DOI</b>	10.3847/1538-4357/ab2637
<b>Handle</b>	<a href="http://hdl.handle.net/20.500.12386/30460">http://hdl.handle.net/20.500.12386/30460</a>
<b>Journal</b>	THE ASTROPHYSICAL JOURNAL
<b>Number</b>	879



# Spectral Energy Distribution of Blue Stragglers in the Core of 47 Tucanae

Silvia Raso<sup>1,2</sup>, Cristina Pallanca<sup>1,2</sup>, Francesco R. Ferraro<sup>1,2</sup>, Barbara Lanzoni<sup>1,2</sup>, Alessio Mucciarelli<sup>1,2</sup>,  
Livia Origlia<sup>2</sup>, Emanuele Dalessandro<sup>2</sup>, Andrea Bellini<sup>3</sup>, Mattia Libralato<sup>3</sup>, and Jay Anderson<sup>3</sup>

<sup>1</sup>Dipartimento di Fisica e Astronomia, Università di Bologna, Via Gobetti 93/2, Bologna I-40129, Italy; [silvia.raso2@unibo.it](mailto:silvia.raso2@unibo.it)

<sup>2</sup>Istituto Nazionale di Astrofisica (INAF), Osservatorio di Astrofisica e Scienza dello Spazio di Bologna, Via Gobetti 93/3, Bologna I-40129, Italy

<sup>3</sup>Space Telescope Science Institute, 3700 San Martin Drive, Baltimore, MD 21218, USA

Received 2019 April 1; revised 2019 May 24; accepted 2019 May 31; published 2019 July 5

## Abstract

We have constructed the spectral energy distributions (SEDs) of a sample of blue straggler stars (BSSs) in the core of the globular cluster 47 Tucanae, taking advantage of the large set of high resolution images, ranging from the ultraviolet to the near-infrared, obtained with the Advanced Camera for Surveys/High Resolution Channel of the *Hubble Space Telescope*. Our final BSS sample consists of 22 objects, spanning the whole color and magnitude extension of the BSS sequence in 47 Tucanae. We fitted the BSS broadband SEDs with models to derive temperature, surface gravity, radius, luminosity, and mass. We show that BSSs indeed define a mass sequence, where the mass increases for increasing luminosity. Interestingly, the BSS mass estimates from the SED fitting turn out to be comparable to those derived from the projection of the stellar position in the color–magnitude diagram on standard star evolutionary tracks. We compare our results with previous, direct mass estimates of a few BSSs in 47 Tucanae. We also find a couple of supermassive BSS candidates, i.e., BSSs with masses larger than twice the turn-off mass, the formation of which must have involved more than two progenitors.

*Key words:* blue stragglers – globular clusters: individual (NGC 104) – techniques: photometric

## 1. Introduction

In the color–magnitude diagram (CMD) of a stellar population, blue straggler stars (BSSs) are a peculiar group of stars that lies along an extrapolation of the main sequence (MS), at brighter magnitudes and bluer colors with respect to the turn-off (TO) point (e.g., Sandage 1953; Ferraro et al. 1992, 1993, 1997, 2004, 2018; Piotto et al. 2004; Lanzoni et al. 2007a, 2007b; Leigh et al. 2007; Dalessandro et al. 2008; Moretti et al. 2008; Beccari et al. 2011, 2012; Simunovic & Puzia 2016). They are the heaviest luminous (nondegenerate) stars in a GC, as suggested by their position in the CMD and as confirmed by a few mass measurements (e.g., Shara et al. 1997; Gilliland et al. 1998; De Marco et al. 2005; Ferraro et al. 2006; Fiorentino et al. 2014; Baldwin et al. 2016; Libralato et al. 2018, 2019). They essentially mimic a younger population, although in GCs any recent star formation event can be safely excluded. Therefore, to explain their presence we must take into account mechanisms able to increase stellar mass. Two main formation processes have been proposed so far: mass-transfer in binary systems (McCrea 1964) and direct collisions between stars (Hills & Day 1976). Although a few pieces of evidence suggest that both mechanisms can be active simultaneously in the same GC (Ferraro et al. 2009; Dalessandro et al. 2013; Simunovic et al. 2014; Xin et al. 2015; Beccari et al. 2019), a complete understanding of their relative efficiency and their dependence on the parent cluster properties is still lacking (e.g., Ferraro et al. 1995, 2003; Davies et al. 2004; Sollima et al. 2008; Chen & Han 2009; Knigge et al. 2009; Chatterjee et al. 2013; Leigh et al. 2013; Sills et al. 2013).

However, irrespective of their origins, BSSs have been demonstrated to be very powerful indicators of GC internal dynamics (Ferraro et al. 2012, 2018; Lanzoni et al. 2016). This is because they are significantly more massive ( $M_{\text{BSS}} \sim 1.2\text{--}1.3 M_{\odot}$ ) than the average stellar mass in GCs ( $\langle m \rangle \sim 0.4 M_{\odot}$ ), and they are therefore subject to dynamical

friction, which makes them sink toward the cluster center (e.g., Mapelli et al. 2004, 2006). Since dynamical friction primarily depends on the local density (rather than on the BSS mass; e.g., Alessandrini et al. 2014), it affects BSSs orbiting at progressively larger distances from the center, continuously modifying their radial distribution within the host cluster. The comparison between the shape of the BSS radial distribution and that of normal (lighter) cluster stars has thus been used to define the so-called “dynamical clock” (Ferraro et al. 2012) and, more recently, the  $A^+$  parameter (Alessandrini et al. 2016), which allows an empirical ranking of stellar systems based on their dynamical ages, i.e., the stage of internal dynamical evolution they achieved (Lanzoni et al. 2016; Raso et al. 2017; Dalessandro et al. 2018; Ferraro et al. 2018; Li et al. 2019; Singh & Yadav 2019; Sollima & Ferraro 2019). Indeed, by investigating  $\sim 30\%$  of the entire GC population in the Milky Way, a strong correlation has been found between the value of  $A^+$  and the number of current central relaxation times that have occurred since the epoch of cluster formation (Ferraro et al. 2018), thus solidly demonstrating the effectiveness of this parameter as a dynamical indicator. In this respect an accurate knowledge of the BSS mass distribution would be of paramount importance for a precise estimate of the BSS sedimentation timescale, thus allowing an accurate calibration of these empirical tools. Moreover, this would also provide crucial hints for a deeper understanding of the formation mechanisms and evolutionary processes of these puzzling stars. In spite of their importance, BSS masses have been determined only for a few BSSs per clusters (e.g., Shara et al. 1997; Gilliland et al. 1998; De Marco et al. 2005; Fiorentino et al. 2014). These sparse measurements have helped to confirm that BSSs are indeed more massive than MS stars. However, systematic studies aimed at obtaining direct mass estimates for large samples of BSSs, covering the entire extension of the sequence, are still unavailable due to observational difficulties.

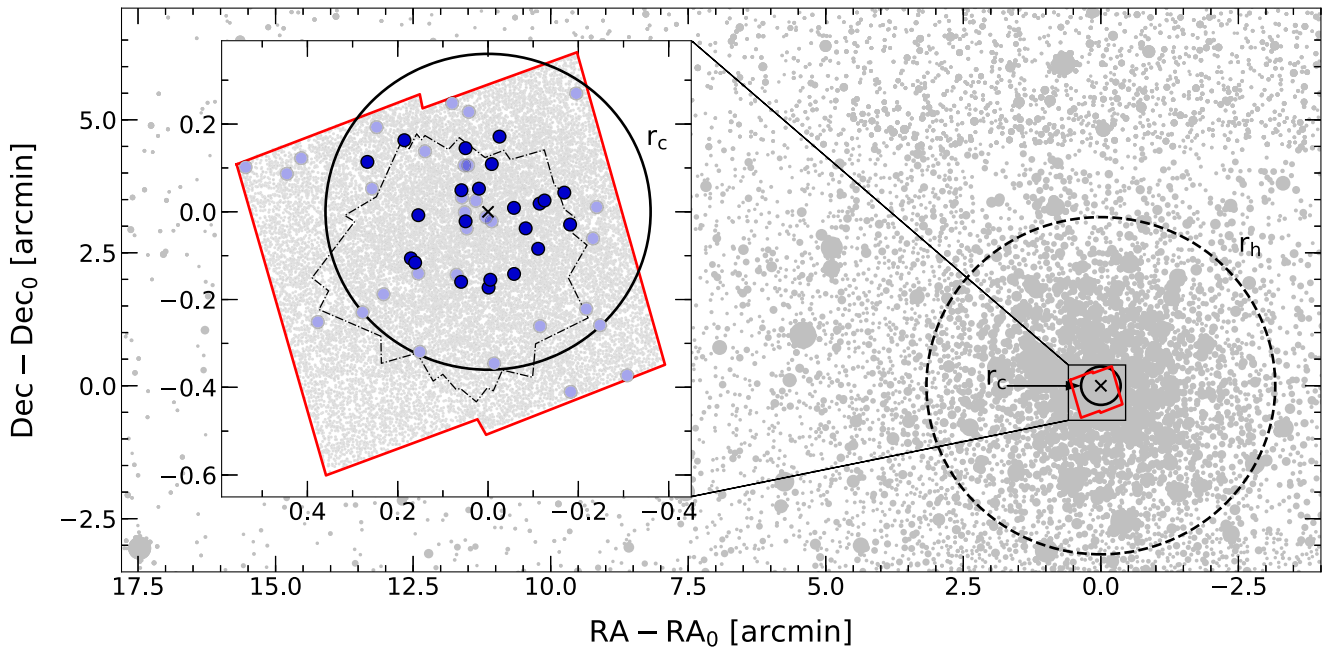


**Figure 1.** Map of the 47 Tuc region analyzed in this work. Positions are in arcminutes, with respect to the cluster center (small black cross). The solid and dashed circles represent the core and half-light radius of the cluster, respectively, from Harris (1996). The red contour marks the FOV of the ACS/HRC data set used in this work. In the inset on the left, we zoom in on the ACS/HRC FOV. The dotted–dashed contour marks the FOV where the time baseline is long enough to measure PMs. The dark blue circles represent the BSSs that survived our selections (as described in Section 3.1), while the light blue circles are all the remaining BSSs detected within the FOV.

BSS mass measurements can be obtained spectroscopically (e.g., Shara et al. 1997; De Marco et al. 2005; see also the recent estimate of the mass of an evolved BSS in 47 Tuc by Ferraro et al. 2016), from pulsational properties (e.g., Gilliland et al. 1998; Fiorentino et al. 2014), or through spectral energy distribution (SED) fitting (e.g., Knigge et al. 2006, 2008; in the latter case, also combined with far-ultraviolet, hereafter FUV, spectroscopy). All these methods require specifically designed observations and techniques: spectroscopic observations must deal with serious crowding issues in the dense environment of GCs, especially in their cores; variability and SED-based studies require *ad hoc* data sets (time-series photometry for the former, and photometry in a large number of filters for the latter), both of which are rarely available in the archives.

The GC 47 Tucanae (47 Tuc, NGC 104) is a notable exception, since it has been intensively studied over the years and has also been used as a calibration field for different *Hubble Space Telescope* (*HST*) instruments. Therefore, a large and multiband set of images of the core of 47 Tuc is publicly available (see Section 2 for a detailed description of the data set). In this work, we use the Advanced Camera for Surveys (ACS) High Resolution Channel (HRC) images in this data set to construct broad (extending from 2000 to 8000 Å) SEDs for a sample of 22 BSSs, distributed along the entire extent of the BSS sequence in 47 Tuc. We used these SEDs to derive BSS physical properties (such as luminosities, masses, radii, etc.).

The paper is organized as follows: in Section 2 we describe the data set and the data reduction procedure; in Section 3 we select the BSS sample and describe the SED-fitting procedure we used; in Section 4 we discuss our results, and in Section 5 we summarize our conclusions.

## 2. Data Set and Data Reduction

The innermost region of 47 Tuc was used as a calibration field for the ACS/HRC, e.g., to study flat-field stability and geometric distortion. For this reason, a large photometric data set is available in the *HST* archive for this region of the sky, which has been repeatedly observed throughout the years of operation of the ACS/HRC (2002–2007). From the archive, we selected all images obtained through broadband filters, which range from the near-UV to the near-infrared (approximately, from 2000 to 8000 Å), thus covering the whole spectral extension of a typical BSS. The total field of view (FOV) covered by this data set is shown in Figure 1 (red contour), compared to the core and half-light radii of the cluster (0.36 and 3.17 arcmin, respectively; Harris 1996). In Table 1 we list the images used for this study; our final data set consists of 285 images. Nearly the same data were used by Knigge et al. (2006, 2008) to study exotic objects such as cataclysmic variables, white dwarfs (WDs), and BSSs. In particular, physical parameters of three BSSs were obtained from spectra and SED fitting. We compare their results with ours in Section 4.1.

The photometric reduction was performed on the `_flt` exposures, because the un-resampled pixel data for stellar profile fitting is preserved. We followed the procedures described in Bellini et al. (2017, 2018), which we briefly summarize in the following.

First, we performed one-pass photometry on the images. This consisted of a single finding procedure without neighbor subtraction. For this step, we determined a spatially variable point-spread function (PSF) model from each individual exposure by examining the residuals from the fit of an empirical library PSF (see Anderson & King 2004) to the bright, relatively isolated, unsaturated stars in that exposure. We then used this tailor-made PSF to measure stellar positions

**Table 1**  
List of *HST* ACS/HRC Observations of 47 Tuc Used in This Work

Program ID	PI	Epoch (yyyy/mm)	Filter	Exposures $N \times t_{\text{exp}}$
9019	R. Bohlin	2002 Apr	F220W	21 × 170 s
			F330W	18 × 66 s
			F435W	2 × 5 s, 2 × 20 s, 17 × 60 s, 2 × 300 s
			F475W	10 × 60 s
			F555W	14 × 60 s
			F606W	10 × 60 s
			F625W	10 × 60 s
			F775W	13 × 60 s
			F814W	2 × 5 s, 2 × 20 s, 14 × 60 s
9028	G. Meurer	2002 Apr	F475W	40 × 60 s
9443	I. King	2002 Jul	F250W	1 × 230 s, 1 × 460 s
			F330W	1 × 350 s
			F435W	1 × 350 s
			F475W	20 × 60 s
9662	R. Gilliland	2002 Sep	F606W	2 × 1 s
10055	J. Biretta	2004 Feb	F250W	2 × 50 s
			F330W	2 × 40 s
			F435W	2 × 20 s
			F606W	2 × 10 s
			F775W	2 × 10 s
10375	J. Mack	2004 Dec; 2005 Mar; 2005 Jun; 2005 Oct	F435W	4 × 60 s
			F475W	4 × 60 s
			F555W	4 × 60 s
			F606W	4 × 60 s
			F625W	4 × 60 s
			F775W	4 × 60 s
			F814W	4 × 60 s
10737	J. Mack	2006 Mar; 2006 May; 2006 Jul	F330W	2 × 66 s
			F435W	6 × 60 s
			F475W	6 × 60 s
			F555W	6 × 60 s
			F606W	6 × 60 s
			F625W	6 × 60 s
			F775W	6 × 60 s
			F814W	6 × 60 s

and fluxes in each exposure. We corrected stellar positions for geometric distortion using the distortion solutions provided by Anderson & King (2004).

Second, since we are focusing on the central, most crowded regions of the cluster, we used a multipass photometric procedure, which is able to perform neighbor subtraction. We used the stellar positions in the early release catalog from the *HST* UV Legacy Survey of Galactic Globular Clusters (Piotto et al. 2015; Soto et al. 2017) as an absolute astrometric reference system. Based on these R.A. and decl. positions, we defined a common, pixel-based reference system, with the  $X$  and  $Y$  axes increasing, respectively, toward west and north, and with the center of the cluster arbitrarily placed at position (5000, 5000). We set the pixel scale to be  $25 \text{ mas pixel}^{-1}$ , consistent with that of ACS/HRC. We transformed each stellar position from the single-exposure, one-pass photometry catalogs into the reference frame by means of six-parameter linear transformations, using a subset of bright, unsaturated and well-measured stars in common between the two catalogs. We rescaled the instrumental magnitudes of each exposure to

match those of the longest available exposures taken with that filter.

The multipass photometry was performed with the code `KS2` (see Bellini et al. 2017 for details). `KS2` combines the results of the one-pass photometry, transformed into the common reference frame, and it is able to simultaneously analyze multiple images of a given stellar field obtained with different filters. For this study, differently from the UV-driven approach adopted in Raso et al. (2017), we performed the finding procedure simultaneously on all the available exposures. This different approach is motivated by the necessity of detecting and subtracting all the potential contaminants (even faint red stars) that can potentially affect the SED of each selected BSS. Note that in the case of the data analyzed here, crowding is reduced because of the very high angular resolution of the ACS/HRC and the relative proximity of the cluster ( $D = 4.5 \text{ kpc}$ , Harris 1996).

`KS2` also provides a set of photometric quality parameters that can be used to select well-measured stars (see Bellini et al. 2017 for a complete description). Briefly, these parameters are the `QFIT` parameter, which indicates the quality of the PSF fit;

**Table 2**  
List of Photometric Calibration Values

Filter	$\Delta\text{mag}$	$\epsilon_{\Delta\text{mag}}$	$ZP_f$
F220W	5.336	0.029	21.883
F250W	5.782	0.042	22.261
F330W	4.407	0.025	22.913
F435W	4.342	0.030	25.188
F475W	4.398	0.074	25.635
F555W	4.391	0.054	25.261
F606W	4.433	0.056	25.906
F625W	4.394	0.062	25.210
F775W	4.305	0.051	24.568
F814W	4.297	0.078	24.856

the  $o$  parameter, which measures the neighbor flux (normalized to the star flux) that had to be subtracted within the fitting radius; and the RADXS parameter, which measures the source flux beyond the fitting radius, with respect to the flux predicted by the PSF. The RADXS parameter is useful to distinguish between extended sources, like galaxies or blends, which have a substantial excess of flux outside the fitting radius with respect to the PSF, and cosmic rays or hot pixels, which have less flux in the outskirts of their profiles with respect to the PSF predictions.

Our data set covers a time baseline of about 4 yr, long enough to measure proper motions (PMs), in order to separate cluster stars from field stars. We measured PMs using the technique developed in Bellini et al. (2014) and recently improved in Bellini et al. (2018). The region where PMs can be measured is smaller than the FOV of the whole data set (see the dashed-dotted contour in the inset of Figure 1), because the external regions were only observed in one epoch (as part of the observing programs 9019 and 9028 performed in 2002).

### 2.1. Photometric Calibration

Since the main goal of this work is to obtain broadband SEDs for a sample of BSSs and use them to estimate their physical parameters, a careful photometric calibration is required. Following the prescriptions given in Bellini et al. (2017), we obtained VEGAMAG calibrated magnitudes from our instrumental magnitudes as follows:

$$m_{f,\text{CAL}} = m_{f,\text{INSTR}} + \Delta\text{mag} + ZP_f, \quad (1)$$

where  $m_{f,\text{CAL}}$  is the calibrated magnitude in the VEGAMAG system in the considered filter  $f$ ;  $m_{f,\text{INSTR}}$  is the instrumental magnitude resulting from the multipass photometry;  $\Delta\text{mag}$  is the  $2.5\sigma$  clipped median difference between the aperture photometry  $m_{\text{AP}}(\lambda)$  and the instrumental magnitudes;  $ZP_f$  is the photometric zero-point of the filter considered.<sup>4</sup> The value  $m_{\text{AP}}(\lambda)$  is measured on the `_drz` images using aperture photometry with a 6 pixel radius and corrected for the finite aperture using the encircled energy values listed in Bohlin (2016). We chose to use a 6 pixel aperture because it represents the best compromise between the need to minimize the contribution of nearby stars and the need for a large aperture. In Table 2 we list the values of  $\Delta\text{mag}$ , with their errors  $\epsilon_{\Delta\text{mag}}$ , and  $ZP_f$  used in this work.

<sup>4</sup> The photometric zero-points were obtained using the ACS zero-points calculator available at <https://acszeropoints.stsci.edu/>.

In order to compute the global photometric error for each star, we combined (in quadrature) the rms of the stellar mean magnitude with the uncertainties of the calibration process. The dominant component in the calibration error budget comes from the  $\Delta\text{mag}$  rms, which is of the order of  $10^{-2}$ – $10^{-1}$  mag, while we neglected a minor possible contribution (of the order of  $10^{-3}$  mag) due to the variation of the  $ZP_f$  as a function of time.

## 3. BSS Selection and SED-fitting Procedure

### 3.1. BSS Selection

Various studies have shown that BSSs in 47 Tuc are concentrated toward the cluster center, as expected for a population of stars heavier than the average (e.g., Paresce et al. 1991; Guhathakurta et al. 1992; de Marchi et al. 1993; Ferraro et al. 2001, 2004, 2012; Parada et al. 2016). Hence, a significant sample of BSSs is expected to fall in the studied FOV, which probes the innermost  $50 \times 50$  arcsec<sup>2</sup> of the cluster (see Figure 1).

We used an ultraviolet CMD ( $m_{\text{F220W}}$  versus  $m_{\text{F220W}} - m_{\text{F330W}}$ ) to select BSSs (similar to the approach used in Ferraro et al. 2001; Raso et al. 2017). In these UV filters, BSSs are among the brightest objects in the cluster, and they define a clear, almost vertical sequence, easily distinguishable from other stellar populations. We selected as BSSs all the 53 stars that fall within the dashed box reported in Figure 2.

Only a subsample of the selected BSSs, represented as dark blue circles in Figure 2, has been used to study the SEDs. First of all, we rejected stars that were detected in fewer than 8 out of the 10 available bandpasses, in order to have a significant number of spectral points for the SED-fitting procedure (see Section 3.3). We also excluded from our sample stars that were measured in fewer than two single exposures per filter, in an effort to include in the final sample only BSSs with robustly measured magnitudes. A further selection was performed by using the quality parameters obtained from the reduction software (described in Section 2). For each BSS, we computed the median value, over all the filters available, of the photometric error, QFIT and RADXS parameters. These median values do not have a real physical meaning, because they are averaged over different filters, but still they provide an overall photometric quality assessment. For example, an extended source should have a large RADXS value regardless of the filter. We thus computed the median and the relative error of the three parameters for all the 53 BSSs in our sample, and we assumed these values in order to select well-measured BSSs by rejecting any star having at least one parameter exceeding  $5\sigma$  the mean value. We arbitrarily assumed  $o = 0.2$  (i.e., the median neighbor flux subtracted before measuring the star was equal to 20% of the star flux itself) as our fixed rejection threshold, to safely exclude stars with bright neighbors.

We also checked the cluster membership of the selected BSSs. We show in Figure 3 the vector-point diagram (VPD) for all the stars with a valid PM measurement (black points). As expected, the figure shows a well-defined clump of stars (indicating the cluster members) with essentially no evidence of field contamination: this was somehow expected, because the observations sampled the innermost regions of the cluster. For reference, the red circle in Figure 3 corresponds to 5 times the central velocity dispersion of bright stars in 47 Tuc

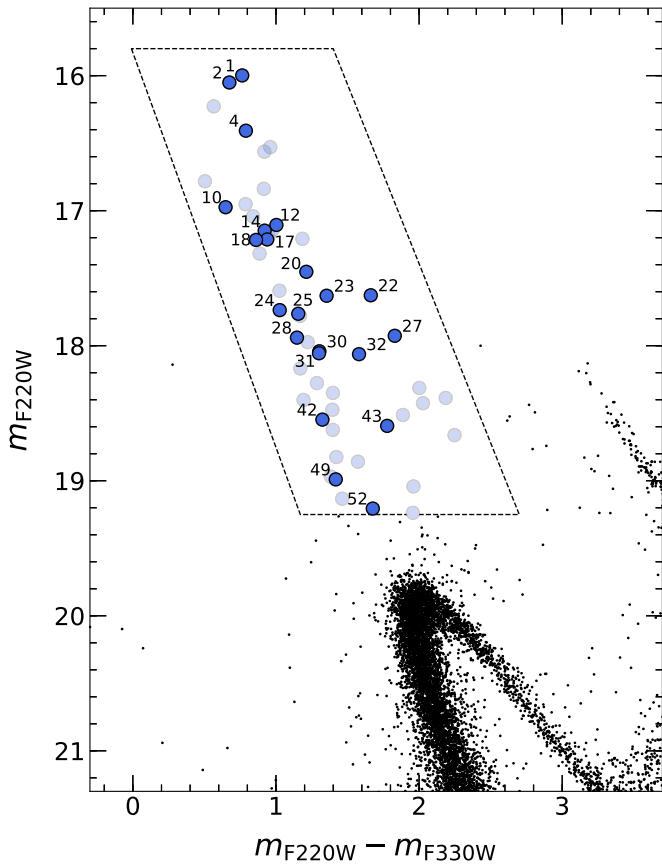


**Figure 2.** UV CMD ( $m_{F220W}$  vs.  $m_{F220W} - m_{F330W}$ ) of the central region of 47 Tuc. The dashed box define the region where we selected BSSs. The blue circles (both light and dark) are the complete sample of BSSs in our data set (53 objects), while the dark blue circles represent the cleaned BSS sample (22 objects, see the text for details on the selection). The dark blue circles are labeled as in Table 3.

( $0.573 \text{ mas yr}^{-1}$ , or  $12.2 \text{ km s}^{-1}$ ; Watkins et al. 2015; Baumgardt & Hilker 2018). Since the FOV where PMs can be measured is smaller than the FOV of the whole data set (see Figure 1), we can provide PM information for only 34 (out of 53) BSSs in our sample (both the light and dark blue circles in Figure 3; the dark blue circles represent BSSs that also survived the quality and variability selection). All of these 34 BSSs are cluster members, as can be seen from Figure 3. Given the negligible level of field contamination, also the remaining 19 BSSs, for which we do not have a PM measurement, have a high probability of being cluster members.

### 3.2. Variability

Variable stars should be excluded from the final BSS sample to avoid the construction of SEDs using magnitudes measured at different phases of variability. The BSS sequence crosses the classical instability strip, so we expect that a few BSSs in our sample could be pulsating variables (e.g., SX Phoenicis). Moreover, some of them are known or suspected eclipsing variables or contact binaries (e.g., W Uma variables). Hence, to perform a meaningful comparison with theoretical SEDs, we excluded all variable BSSs by cross-correlating the BSS positions in our catalog with the positions of variable objects listed in the catalog of Variable Stars in Galactic Globular

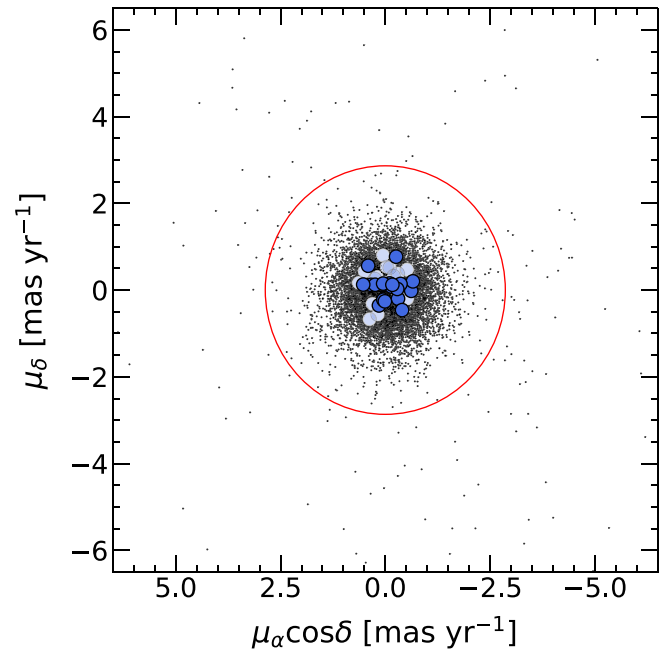


**Figure 3.** Vector-point diagram for all the stars with a PM measurement in our data set (black points). The blue circles (color coded as in Figure 2) correspond to the 34 BSSs for which PMs could be measured. The red circle corresponds to 5 times the central velocity dispersion of bright stars in 47 Tuc, plotted as a reference.

Clusters (Clement et al. 2001, last update for 47 Tuc: 2017 January<sup>5</sup>), to identify the already known or suspected variables (both eclipsing and pulsating). We focused our attention on variables from Edmonds et al. (1996) and Gilliland et al. (1998), who studied variability in the central  $66 \times 66 \text{ arcsec}^2$  of 47 Tuc with adequate *HST* photometry, and we finally identified nine objects.

In summary, 9 BSSs have been excluded due to variability, 16 because they have been measured in too few bandpasses (or because only a few exposures were available per filter), and 6 because of the photometric quality selection. Therefore, the final, quality-selected and variable-cleaned BSS sample consists of 22 stars (the dark blue dots in Figures 1–3), which still covers the whole magnitude and color ranges of the observed BSS sequence, thus allowing us to study this population in its entirety. Of the 22 BSSs from the clean sample, 18 have a PM measurement, which allowed us to definitely confirm that they are cluster members.

### 3.3. SED Fitting

We first corrected the observed magnitudes for reddening, adopting the following relation:

$$m_{f,\text{corr}} = m_{f,\text{obs}} - c_f R_V E(B - V), \quad (2)$$

where, for each bandpass  $f$ ,  $m_{f,\text{corr}}$  is the reddening-corrected magnitude;  $m_{f,\text{obs}}$  is the original observed magnitude;  $c_f = A_\lambda/A_V$  is the extinction law (Cardelli et al. 1989);  $R_V = 3.12$  is the extinction coefficient; and  $E(B - V) = 0.04$  is the reddening value for 47 Tuc (Harris 1996).

We then constructed model SEDs as follows. We produced a grid of synthetic spectra with temperature and surface gravity

<sup>5</sup> The catalog is available at <http://www.astro.utoronto.ca/~cclement/cat/C0021m723>.

ranges appropriate for BSSs:  $5000 \text{ K} < T_{\text{eff}} < 10,000 \text{ K}$  with a step of  $100 \text{ K}$ ;  $3 < \log(g) < 5$  with a step of  $0.1$ . All the synthetic spectra were calculated with the software `SYNTHE` (Sbordone et al. 2004; Kurucz 2005). For each point of the grid, a one-dimensional, plane-parallel, LTE model atmosphere has been calculated with the code `ATLAS9` (Kurucz 2005), adopting  $[\text{Fe}/\text{H}] = -0.70$  dex and an  $\alpha$ -enhanced chemical mixture<sup>6</sup> (Dotter et al. 2010). The spectral synthesis was performed in the wavelength range between  $1000$  and  $10000 \text{ \AA}$ , including all the atomic and molecular lines available in the Kurucz/Castelli database,<sup>7</sup> with the exclusion of TiO lines that are negligible for the investigated range of stellar parameters. Finally, each spectrum has been convolved with a Gaussian profile in order to obtain a spectral resolution of  $1000$ . The flux of synthetic spectra  $F(\nu)$  is in units of  $\text{erg cm}^{-2} \text{ s}^{-1} \text{ Hz}^{-1} \text{ sr}^{-1}$ . We converted it into apparent flux  $f(\lambda)$  (in flam units, i.e.,  $\text{erg cm}^{-2} \text{ s}^{-1} \text{ \AA}^{-1}$ ) as follows:

$$f_{\lambda} = \frac{4\pi c}{\lambda^2} \left( \frac{R}{D} \right)^2 F(\nu), \quad (3)$$

where  $c = 3 \times 10^{10} \text{ cm s}^{-1}$  is the speed of light;  $R$  is the star radius (defined by a grid in the range:  $0.1 R_{\odot} < R < 4.5 R_{\odot}$ , with a step of  $0.01 R_{\odot}$ ); and  $D$  is the cluster distance. We converted the apparent fluxes to synthetic, apparent magnitudes  $m_{f,\text{syn}}$  (in the VEGAMAG system, to match our observed, calibrated magnitudes), by convolution with the filter throughputs, using the `pysynphot` package (Lim et al. 2015).

We then directly compared observed and model SEDs. It is important to note that our model grid consists only of single star models, so we assume that all the BSSs in our sample are single stars. This assumption should be reasonably safe, because we have already excluded from the considered sample all the BSSs known or suspected to be eclipsing variables (see Section 3.2). Moreover, the presence of BSSs with a degenerate companion (i.e., a WD) should not affect our results, because the WD emission is expected to be too hot and faint to significantly affect even the flux measured with the bluest filter.

We performed the fit using a Markov chain Monte Carlo (MCMC) approach, based on the `emcee` algorithm (Foreman-Mackey et al. 2013). We thus obtained the posterior probability distribution function (PDF) for each parameter of the fit ( $T_{\text{eff}}$ ,  $\log(g)$ ,  $R$ ) and subsequently derived the posterior PDF also for mass ( $M$ ) and luminosity ( $L$ ) through the following equations:

$$g = \frac{GM}{R^2}; \quad L = 4\pi R^2 \sigma T_{\text{eff}}^4, \quad (4)$$

where  $G = 6.67 \times 10^{-8} \text{ g}^{-1} \text{ cm}^3 \text{ s}^{-2}$  is the gravitational constant, and  $\sigma = 5.7 \times 10^{-5} \text{ erg cm}^{-2} \text{ s}^{-1} \text{ K}^{-4}$  is the Stefan–Boltzmann constant. Since the priors we assumed are uniform, the posterior PDFs are proportional to the likelihood  $L = \exp(-\chi^2/2)$ . We computed  $\chi^2$  as:

$$\chi^2 = \sum_f \left( \frac{\Delta m}{\sigma_{f,\text{obs}}} \right)^2 + \left( \frac{\Delta m_{UB,\text{corr}} - \Delta m_{UB,\text{syn}}}{\sigma_{UB,\text{obs}}} \right)^2, \quad (5)$$

where the sum is performed over the 10 bandpasses used to construct the SEDs;  $\Delta m = m_{f,\text{corr}} - m_{f,\text{syn}}$  is the difference

<sup>6</sup> We tested if a small  $[\text{Fe}/\text{H}]$  variation ( $\sim 0.1$  dex) or a solar-scaled (instead of  $\alpha$ -enhanced) chemical mixture could significantly affect our results, and we found that the impact on the derived synthetic magnitudes is negligible.

<sup>7</sup> <http://wwwuser.oats.inaf.it/castelli/linelists.html>

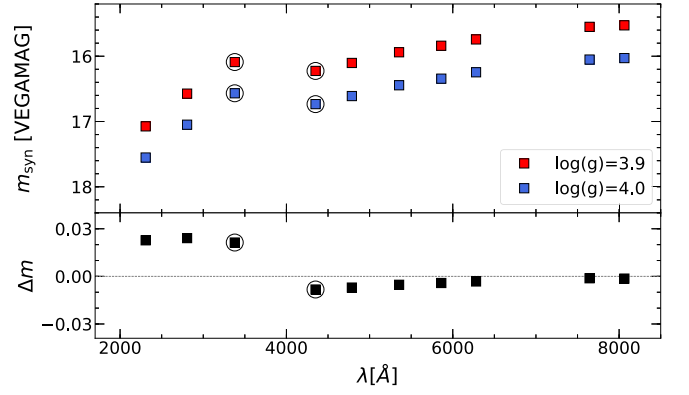


**Figure 4.** Top panel: synthetic magnitudes for two values of  $\log(g)$ , differing only by  $0.1$  dex (see the legend), while temperature and radius are fixed ( $T_{\text{eff}} = 7000 \text{ K}$ ,  $R = 2.5 R_{\odot}$ , respectively). The  $\log(g) = 4.0$  model is shifted by  $0.5$  mag fainter for clarity. Bottom panel: the black squares correspond to the difference between the two models plotted in the top panel. As can be seen, although the difference between the two models is quite small (of the order of a few hundredths of magnitude), it is positive at wavelengths shorter than  $\approx 4000 \text{ \AA}$ , and negative afterwards, changing sign abruptly. The quantity  $\Delta m_{UB,\text{syn}} = m_{F330W,\text{syn}} - m_{F435W,\text{syn}}$ , defined in Section 3.3, has been introduced to maximize the sensitivity of the fit to this spectral region, where the dependence of the models on surface gravity is higher.  $m_{F330W,\text{syn}}$  and  $m_{F435W,\text{syn}}$  are, respectively, the third and fourth squares from the left, circled for clarity.

between the observed, dereddened magnitudes and the synthetic ones;  $\sigma_{f,\text{obs}}$  is the error associated with the observed magnitudes (see Section 2.1).  $\Delta m_{UB,\text{corr}} = m_{F330W,\text{corr}} - m_{F435W,\text{corr}}$  is the observed magnitude difference (i.e., color) between the observed, dereddened magnitudes in the F330W and F435W bandpasses (roughly corresponding to Johnson  $U$  and  $B$  filters),  $\Delta m_{UB,\text{syn}} = m_{F330W,\text{syn}} - m_{F435W,\text{syn}}$  is the equivalent quantity for synthetic magnitudes, while  $\sigma_{UB,\text{obs}}$  is the error associated to  $\Delta m_{UB,\text{corr}}$ , obtained by adding in quadrature  $\sigma_{F330W,\text{obs}}$  and  $\sigma_{F435W,\text{obs}}$ , i.e., the errors associated to the observed magnitudes in these two bandpasses. The aim of this last term of the  $\chi^2$  is to increase the sensitivity of the fit to surface gravity. As can be seen in Figure 4, surface gravity has quite a weak impact on the SEDs. However, the spectral region sampled by the F330W and F435W filters (i.e., around the Balmer jump region; circled squares in Figure 4) seems instead to be sensitive to the adopted gravity. Increasing the fit sensitivity to surface gravity is particularly important for two reasons: first, the surface gravity grid is defined in logarithmic units; therefore, small uncertainties in  $\log(g)$  translate into significant variations of the surface gravity. Second, mass is directly proportional to surface gravity; therefore, the goodness of the fit on surface gravity directly influences the accuracy of the mass determination.

The results of the fitting procedure are listed in Table 3. The best-fit values for each parameter correspond to the PDF median, while the reported uncertainties correspond to the 68% confidence interval. In Figure 5 we show the SEDs of a bright, an intermediate-magnitude, and a faint BSS, namely BSS4, BSS18, and BSS52, overplotted to the corresponding best-fit model. In the lower panels we show the residuals between the observed SED and the best-fit model. It can be seen that, in any case, the residuals are small and that observed SEDs and models are in good agreement within the errors.

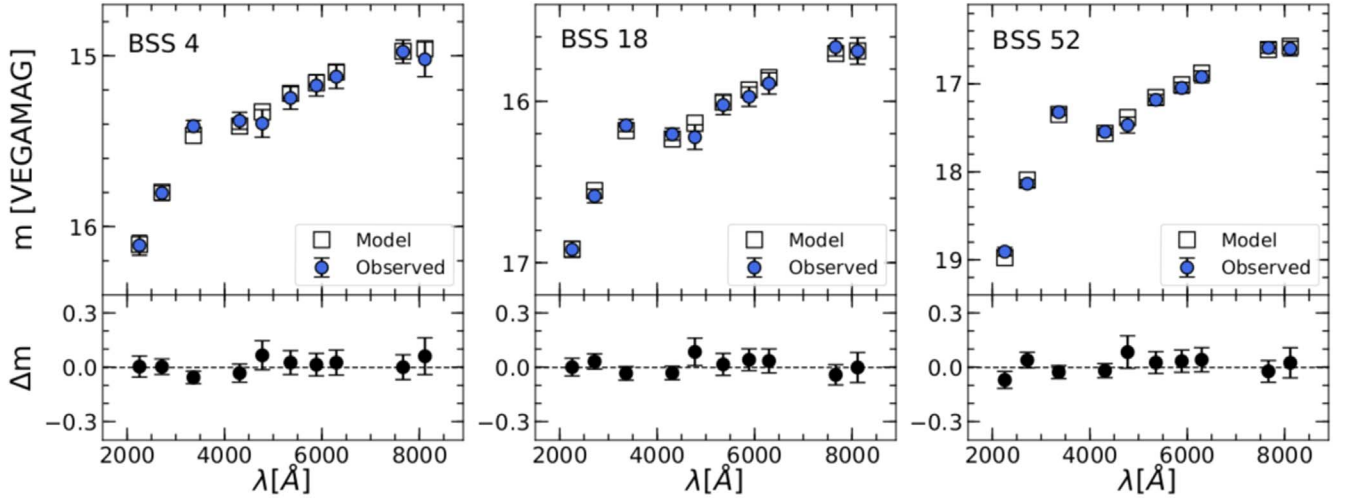


**Figure 5.** Top panels: observed SEDs of three BSSs from our sample, namely BSS4, BSS18, and BSS52 (blue circles), overplotted to the corresponding best-fit model (empty squares; see Table 3). Bottom panels: residuals between the observed SED and the best-fit model.

**Table 3**  
Best-fit Parameters for the Clean BSS Sample

BSS ID	$T$ [K]	$\log(g)$	$R$ [ $R_{\odot}$ ]	$L$ [ $L_{\odot}$ ]	$M$ [ $M_{\odot}$ ]
BSS1	$7600^{+80}_{-90}$	$3.70^{+0.11}_{-0.13}$	$3.51^{+0.11}_{-0.09}$	$35.9^{+0.8}_{-0.8}$	$2.31^{+0.64}_{-0.59}$
BSS2	$7900^{+90}_{-90}$	$3.63^{+0.09}_{-0.07}$	$2.99^{+0.08}_{-0.08}$	$30.7^{+0.7}_{-0.7}$	$1.39^{+0.35}_{-0.22}$
BSS4	$7600^{+110}_{-110}$	$3.79^{+0.12}_{-0.11}$	$2.92^{+0.09}_{-0.09}$	$24.7^{+0.6}_{-0.6}$	$1.93^{+0.57}_{-0.45}$
BSS10	$7800^{+130}_{-130}$	$4.08^{+0.11}_{-0.11}$	$1.95^{+0.06}_{-0.07}$	$12.5^{+0.3}_{-0.3}$	$1.68^{+0.56}_{-0.40}$
BSS12	$7100^{+90}_{-50}$	$3.72^{+0.10}_{-0.10}$	$2.67^{+0.04}_{-0.08}$	$15.9^{+0.4}_{-0.3}$	$1.36^{+0.33}_{-0.31}$
BSS14	$7200^{+90}_{-90}$	$3.90^{+0.11}_{-0.13}$	$2.39^{+0.07}_{-0.06}$	$13.8^{+0.4}_{-0.4}$	$1.66^{+0.54}_{-0.43}$
BSS17	$7200^{+50}_{-50}$	$3.74^{+0.09}_{-0.08}$	$2.43^{+0.08}_{-0.03}$	$13.9^{+0.3}_{-0.3}$	$1.19^{+0.27}_{-0.22}$
BSS18	$7400^{+70}_{-80}$	$3.90^{+0.11}_{-0.09}$	$2.17^{+0.06}_{-0.03}$	$12.3^{+0.3}_{-0.3}$	$1.39^{+0.37}_{-0.25}$
BSS20	$6800^{+70}_{-60}$	$3.82^{+0.11}_{-0.10}$	$2.71^{+0.03}_{-0.09}$	$13.8^{+0.4}_{-0.3}$	$1.75^{+0.53}_{-0.38}$
BSS22	$6400^{+50}_{-60}$	$3.41^{+0.11}_{-0.10}$	$3.72^{+0.13}_{-0.04}$	$20.4^{+0.6}_{-0.5}$	$1.29^{+0.38}_{-0.28}$
BSS23	$6700^{+50}_{-70}$	$3.75^{+0.12}_{-0.12}$	$2.75^{+0.10}_{-0.04}$	$13.4^{+0.3}_{-0.3}$	$1.57^{+0.60}_{-0.37}$
BSS24	$7100^{+50}_{-100}$	$4.18^{+0.12}_{-0.10}$	$1.92^{+0.06}_{-0.03}$	$8.2^{+0.2}_{-0.2}$	$2.10^{+0.66}_{-0.45}$
BSS25	$6900^{+70}_{-50}$	$4.00^{+0.12}_{-0.11}$	$2.20^{+0.04}_{-0.06}$	$9.6^{+0.2}_{-0.2}$	$1.76^{+0.56}_{-0.42}$
BSS27	$6200^{+60}_{-50}$	$3.15^{+0.15}_{-0.11}$	$3.82^{+0.06}_{-0.13}$	$18.9^{+0.6}_{-0.5}$	$0.76^{+0.31}_{-0.16}$
BSS28	$6900^{+60}_{-60}$	$4.02^{+0.10}_{-0.11}$	$2.00^{+0.06}_{-0.03}$	$7.9^{+0.2}_{-0.2}$	$1.56^{+0.42}_{-0.35}$
BSS30	$6700^{+90}_{-40}$	$3.83^{+0.11}_{-0.10}$	$2.24^{+0.03}_{-0.06}$	$8.8^{+0.2}_{-0.2}$	$1.22^{+0.34}_{-0.25}$
BSS31	$6700^{+80}_{-60}$	$3.72^{+0.14}_{-0.14}$	$2.21^{+0.03}_{-0.07}$	$8.7^{+0.2}_{-0.2}$	$0.92^{+0.37}_{-0.27}$
BSS32	$6400^{+60}_{-50}$	$3.72^{+0.18}_{-0.19}$	$2.79^{+0.06}_{-0.06}$	$11.4^{+0.4}_{-0.3}$	$1.49^{+0.77}_{-0.54}$
BSS42	$6600^{+70}_{-50}$	$3.93^{+0.11}_{-0.11}$	$1.83^{+0.02}_{-0.06}$	$5.6^{+0.2}_{-0.2}$	$1.03^{+0.30}_{-0.25}$
BSS43	$6200^{+90}_{-20}$	$3.39^{+0.20}_{-0.20}$	$2.65^{+0.05}_{-0.09}$	$9.1^{+0.3}_{-0.3}$	$0.63^{+0.33}_{-0.26}$
BSS49	$6600^{+60}_{-80}$	$3.87^{+0.17}_{-0.16}$	$1.53^{+0.05}_{-0.02}$	$3.9^{+0.1}_{-0.1}$	$0.64^{+0.33}_{-0.20}$
BSS52	$6300^{+80}_{-60}$	$3.84^{+0.18}_{-0.15}$	$1.78^{+0.03}_{-0.06}$	$4.4^{+0.1}_{-0.1}$	$0.79^{+0.45}_{-0.24}$

#### 4. Discussion

In Figure 6 we plot the luminosity and temperature of the selected BSSs in the ( $\log L - \log T_{\text{eff}}$ ) Hertzsprung–Russel (HR) diagram. As a reference, we also plot a 12 Gyr BaSTI isochrone<sup>8</sup> (Pietrinferni et al. 2004; Hidalgo et al. 2018, solid black line) to highlight the TO, sub-giant branch (SGB), red giant branch (RGB), and horizontal branch loci of “normal” stars of the cluster. As expected, the values of temperature and luminosity derived from the SED-fitting result in BSSs standing clearly outside the standard evolutionary loci, defining a sequence along the extrapolation of the cluster MS, with

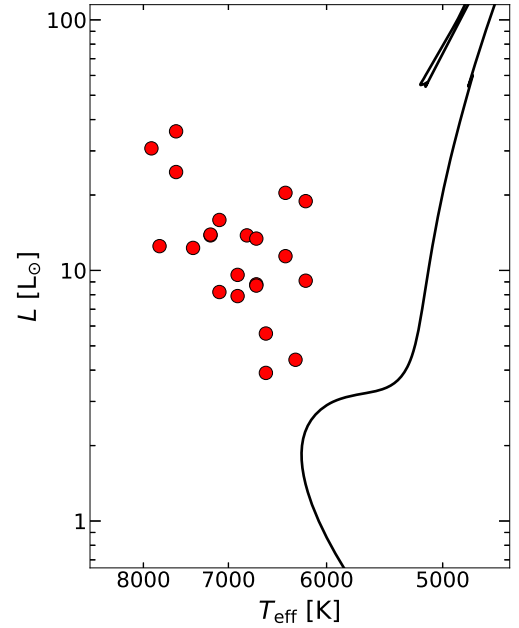


**Figure 6.** Position of the studied BSSs (red circles) in the HR diagram. The black solid line is a 12 Gyr BaSTI isochrone (Pietrinferni et al. 2004; Hidalgo et al. 2018), plotted as a reference to trace the normal TO, SGB, and RGB sequences of the cluster.

luminosities ranging from  $\sim 3$  to  $\sim 30 L_{\odot}$  and temperatures between  $\sim 6000$  to  $\sim 8000$  K.

In Figure 7 we show the distribution of the analyzed BSSs in the UV CMD, in which each BSS is marked with a color code that quantifies the value of the parameters derived from the SED analysis (see labels). As can be seen, the resulting parameters vary according to theoretical predictions. In the first panel, temperature decreases as BSS color increases. In the second and third panels, respectively, surface gravity decreases and radius increases moving away from the zero age main sequence (ZAMS). In the fourth panel, bolometric luminosity increases as a function of the magnitude, but there is also an expected dependence on the color, because at fixed UV magnitudes, the reddest stars have lower temperatures, thus they are brighter at longer wavelengths (i.e., they have larger

<sup>8</sup> <http://basti-iac-ao-abruzzo.inaf.it/index.html>



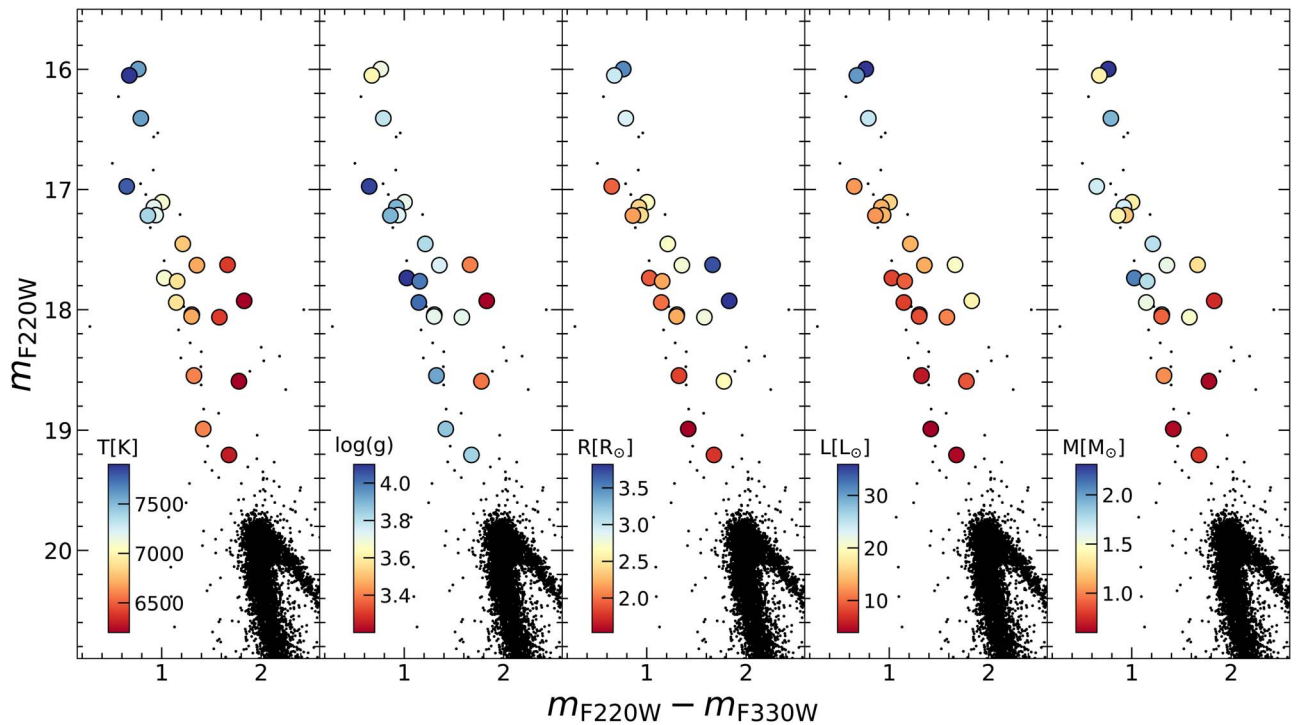


**Figure 7.** Distributions of the best-fit parameters obtained for the clean BSS sample, shown in the CMD. From left to right: temperature, surface gravity (logarithmic units), radius, bolometric luminosity, and mass. Units and colorbars are marked inside each panel.

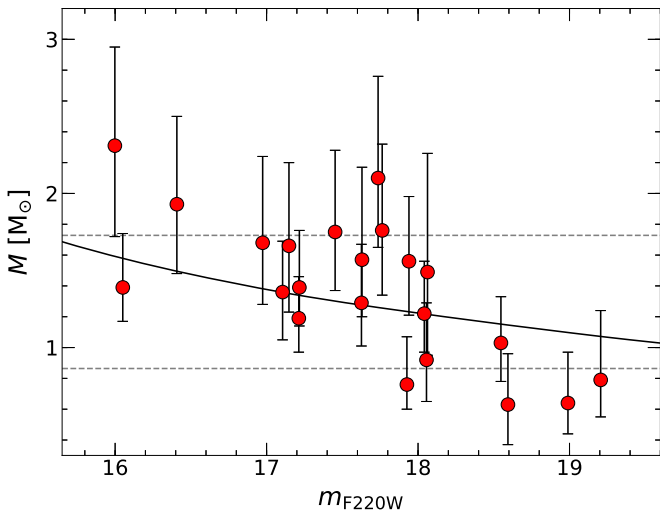


**Figure 8.** Resulting masses, with uncertainties corresponding to the 68% confidence interval, as a function of F220W magnitude (red points). The black solid line is a 100 Myr BaSTI isochrone (Pietrinfermi et al. 2004; Hidalgo et al. 2018) with  $[\text{Fe}/\text{H}] = -0.70$  plotted as a reference. The two horizontal, dashed lines correspond to  $M_{\text{TO}}$  and  $2M_{\text{TO}}$  ( $M_{\text{TO}} \sim 0.86 M_{\odot}$ , from the 12 Gyr BaSTI isochrone reported in Figure 6).

bolometric corrections): hence their bolometric luminosity is larger.

Regarding BSS masses, the distribution shown in the rightmost panel of Figure 7 suggests the presence of a mass succession along the BSS sequence, with lower masses at the faint end and higher masses at the bright end of the sequence. We reiterate, however, that mass errors are quite large (see column 5 of Table 3, and Figure 8) due to the lack of very strong surface gravity tracers in the SEDs, as explained in the

previous section. In spite of this, a mass sequence is also confirmed by the plot in Figure 8, where the BSS masses are plotted as a function of the F220W magnitude. Moreover, the mass distribution seems qualitatively in agreement with that predicted by theoretical ZAMS models: the black line in Figure 8 is a 100 Myr BaSTI isochrone (Pietrinfermi et al. 2004; Hidalgo et al. 2018) with  $[\text{Fe}/\text{H}] = -0.70$ , plotted as a reference for the ZAMS of the cluster. In order to test the statistical significance of the detected BSS mass–magnitude relation, we measured the Spearman and Pearson correlation coefficients. We obtained  $\rho = -0.64$  and  $r = -0.70$ , respectively, supporting the presence of an anticorrelation between mass and magnitude. Note that the mass–magnitude relation is also visible by using different bandpasses, but the adoption of UV filters tends to maximize the magnitude extension of the BSS sequence.

As shown in Figure 8, a few BSSs (specifically BSS1, BSS4, BSS20, BSS24, and BSS25) in our sample have masses larger than  $2M_{\text{TO}}$  (we assumed  $M_{\text{TO}} \sim 0.86 M_{\odot}$ , from the same 12 Gyr BaSTI isochrone reported in Figure 6). The presence of BSSs with twice the MS-TO mass would imply a formation mechanism that involves at least three stars (e.g., Knigge et al. 2006, 2008). However, within the uncertainties, these stars are still compatible with a mass lower than this threshold value; therefore, they are just candidate supermassive-BSSs. It would be interesting to measure the masses of these stars with other direct methods, e.g., spectroscopically (see Ferraro et al. 2016), in order to confirm or reject this hypothesis. The masses derived for four BSSs (specifically BSS27, BSS43, BSS49, and BSS52), turn out to be lower than  $M_{\text{TO}}$ . These values are, however, still compatible with a mass larger than the TO mass within the errors. Most of them are (with the possible exception of BSS27) low-mass faint BSSs: they are clearly distinguishable from the MS only in an UV CMD, as the one used in this

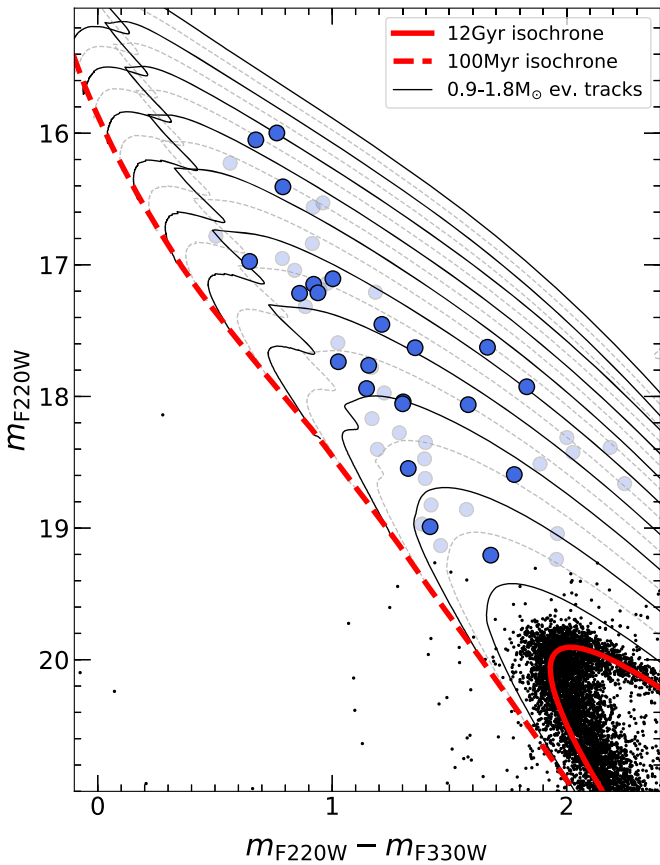


**Figure 9.** UV CMD with the BSS sample highlighted (blue circles; the dark blue ones represent the clean sample). The evolutionary tracks used to estimate the BSS mass ( $M_{\text{TR}}$ , see the text for details) are also plotted. They span the range 0.9–1.8  $M_{\odot}$ , with a step of 0.05  $M_{\odot}$  (alternatively plotted as solid black lines and gray dashed lines for clarity). Two isochrones, of 12 Gyr and 100 Myr, are superposed for reference, respectively, as solid and dashed red lines.

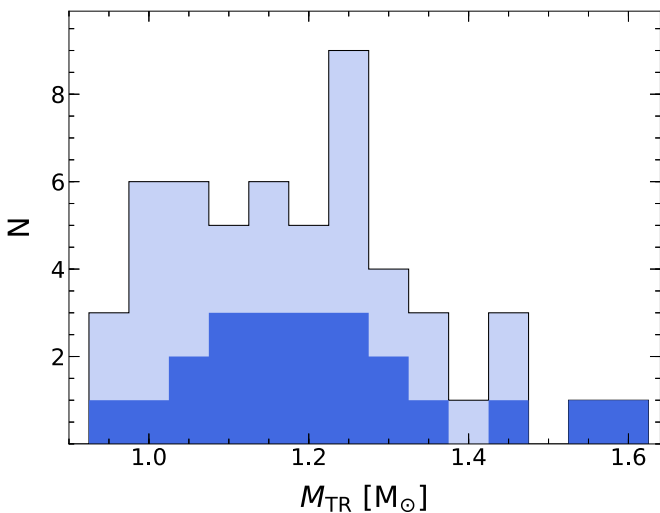


**Figure 10.** Light blue histogram: mass distribution, obtained from the evolutionary tracks, for the entire sample of 53 BSSs. Dark blue histogram: mass distribution, obtained from the evolutionary tracks, for the clean sample of 22 BSSs.

work, while in a classical, optical diagram they do not appear to be significantly different from MS-TO stars (see Raso et al. 2017).

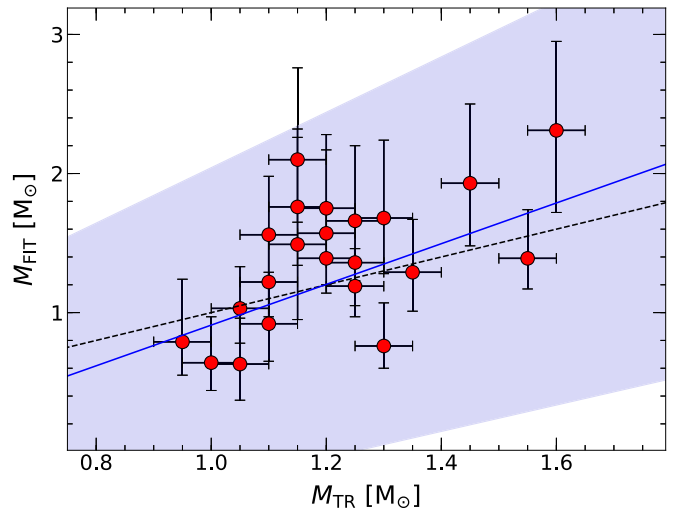


**Figure 11.** Red points: masses resulting from the SED-fitting method, with uncertainties corresponding to the 68% confidence interval, as a function of the masses estimated from evolutionary tracks (see the text for details; the  $M_{\text{TR}}$  uncertainties are equal to 0.05  $M_{\odot}$ , i.e., the step of the evolutionary grid used to measure  $M_{\text{TR}}$  itself). The black, dashed line is the bisector. The blue solid line is the best-fit straight line obtained with a maximum likelihood approach, considering both the y- and x-axis uncertainties (with slope  $a = 1.46^{+0.53}_{-0.52}$  and intercept  $b = -0.55^{+0.60}_{-0.63}$ ). The blue shaded area represents the 68% interval around the best-fit relation.

In general, a comparison with evolutionary tracks can provide a rough estimate of the BSS mass. Here we used a set of isochrones and evolutionary tracks (in the range 0.9–1.8  $M_{\odot}$ ) from the BaSTI model library. The theoretical models have been colored by convolving a grid of suitable Kurucz (1993) stellar spectra of appropriate metallicity with the transmission curves of the used ACS/HRC filters. Thus, for each given stellar temperature and gravity, both the color and the bolometric corrections in the VEGAMAG system have been computed. The set of evolutionary tracks (at  $[\text{Fe}/\text{H}] = -0.7$ ) in the range 0.9–1.8  $M_{\odot}$  are shown in Figure 9, overplotted to the ( $m_{\text{F220W}}$  versus  $m_{\text{F220W}} - m_{\text{F330W}}$ ) CMD: a distance modulus of  $(m - M)_0 = 13.3$  and a color excess  $E(B - V) = 0.04$  have been adopted. Small offsets (of the order of a few 0.01) in color and magnitude have been applied to the evolutionary models in order to allow the 12 Gyr isochrone to perfectly match the MS-TO. The evolutionary tracks at steps of 0.05  $M_{\odot}$  shown in Figure 9 represent the reference “pillars” for the interpolation procedure that allowed us to estimate the mass of each BSS. The derived mass distribution for the entire sample of 53 BSSs is plotted in Figure 10. An average mass of 1.2  $M_{\odot}$ , in agreement with other mass determination in the literature (see Ferraro et al. 2006; Lanzoni et al. 2007b; Fiorentino et al. 2014), is obtained from this sample.

Note that here we have the possibility of directly comparing the BSS masses obtained from the SED-fitting ( $M_{\text{FIT}}$ ) with those obtained from evolutionary tracks ( $M_{\text{TR}}$ ), for the subsample of 22 well-measured BSSs. We report the result of the comparison between  $M_{\text{FIT}}$  and  $M_{\text{TR}}$  in Figure 11. We fitted the points with a straight line using a maximum likelihood approach, equivalent to the one described in Section 3.3, considering both the y- and x-axis uncertainties. We obtained a slope  $a = 1.46^{+0.53}_{-0.52}$  and an intercept  $b = -0.55^{+0.60}_{-0.63}$  (the blue solid line in Figure 11). In the figure we also plotted, as a reference, the bisector line (black dashed line) i.e., a straight

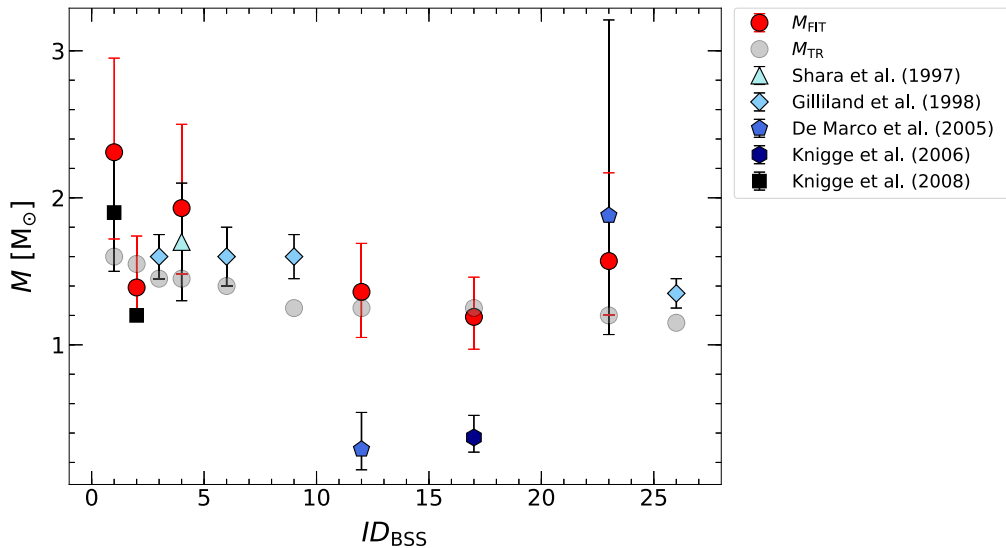


**Figure 12.** BSS masses obtained from our SED-fitting method (red circles) and from the comparison with evolutionary tracks (gray circles), plotted against the BSS ID, compared to the values quoted in the literature for the same objects (points with different shades of blue, see the legend).

line with slope  $a = 1$  and intercept  $b = 0$ , which represents the full correspondence between the  $M_{\text{FIT}}$  and  $M_{\text{TR}}$  values. As can be seen, the best-fit relation turns out to be in reasonable agreement with the bisector. Therefore, we can conclude that, when a direct BSS mass estimate cannot be made, the evolutionary track method can be used to provide a reasonable first-guess estimate of the BSS mass.

#### 4.1. Comparison with Previous Mass Estimates

A few direct mass measurements of BSSs in the core of 47 Tuc are already available in the literature. In this section, we compare our results with previous estimates. The results of this comparison are summarized in Figure 12.

The first direct BSS mass measurement was indeed obtained on a 47 Tuc BSS by Shara et al. (1997), comparing an *HST* spectrum (obtained with the Faint Object Spectrograph) with model spectra, and finding  $M = 1.7 \pm 0.4 M_{\odot}$  (light blue triangle in Figure 12). The BSS they studied corresponds to our BSS4. The mass we obtain for this object is  $M = 1.93^{+0.57}_{-0.45} M_{\odot}$  (see Table 3), which is fully compatible, within the errors, with the value obtained spectroscopically by Shara et al. (1997).

Gilliland et al. (1998) measured the masses of four variable BSSs in 47 Tuc on the basis of their pulsations (specifically V2, V14, V15, V16). They found masses equal to:  $1.6 \pm 0.2 M_{\odot}$ ,  $1.35 \pm 0.1 M_{\odot}$ ,  $1.6 \pm 0.15 M_{\odot}$ ,  $1.6 \pm 0.15 M_{\odot}$ , respectively (light blue diamonds in Figure 12). We indeed detected in our FOV the four BSSs studied in Gilliland et al. (1998), which correspond to BSS6, BSS26, BSS3 and BSS9, respectively. We did not estimate their mass through SED fitting, since we excluded from this study all the known or suspected variables (see Section 3.2). However, we can compare the values reported in Gilliland et al. (1998) with the masses we obtained from evolutionary tracks. Specifically, our  $M_{\text{TR}}$  values for these four objects are:  $1.40 M_{\odot}$ ,  $1.15 M_{\odot}$ ,  $1.45 M_{\odot}$ , and  $1.25 M_{\odot}$ . As can be seen, the values for BSS3 and BSS6 are compatible with the values from Gilliland et al. (1998), while for BSS9 and BSS26 the masses from their work are slightly larger. However, estimating masses from evolutionary tracks could be less efficient for variable stars, because

these kinds of objects slightly change position in the CMD depending on the phase of the variability.

De Marco et al. (2005) spectroscopically obtained masses and rotation rates of 55 stars (including 24 BSSs) in four GCs, including 47 Tuc. In particular, they analyzed 5 BSSs in 47 Tuc (see their Table 4). We detected all five of these objects in our sample, but only two of them pass our quality/variability conditions and therefore they have been analyzed in this work. Namely, their star NGC 104-5 corresponds to our BSS12 and their NGC 104-7 corresponds to our BSS23. They obtain masses equal to  $0.29^{+0.25}_{-0.14} M_{\odot}$  and  $1.88^{+1.33}_{-0.81} M_{\odot}$ , respectively (blue pentagons in Figure 12), while we obtain  $1.36^{+0.33}_{-0.31} M_{\odot}$  and  $1.57^{+0.60}_{-0.37} M_{\odot}$ , respectively. The two mass values for BSS23 are fully compatible within the errors, while those of BSS12 are not, with their mass estimate being significantly smaller than ours. The spectrum of this star has a high S/N ratio but is affected by blending (see Section 7.2 in De Marco et al. 2005). The authors also discuss a temperature inconsistency between the low- and the intermediate-resolution spectra (see their Section 11). These can be two possible explanations for the discrepancy between the two mass measurements.

Knigge et al. (2006, 2008) obtained physical parameter estimates for a few BSSs in the core of 47 Tuc using almost the same data set as ours (excluding the ACS/HRC F220W images and including the ACS/HRC F850LP and STIS F25QTZ images, and also FUV spectroscopy in the latter work) and the same technique, i.e., SED fitting, albeit using a least squares approach.

In Knigge et al. (2006), they identify the star BSS7 (dark blue hexagon in Figure 12; nomenclature from Paresce et al. 1991; hereafter, to avoid confusion with our nomenclature, we will name this star K-BSS7) as the optical counterpart to the *Chandra* X-ray source W31 (Grindlay et al. 2001). They found K-BSS7 to be variable, but with a very small amplitude ( $A_V = 0.0037$  mag). K-BSS7 corresponds to BSS17 in this work. Given its very small variability amplitude, BSS17 survived the selection criteria discussed in Section 3.2 and has been kept in our final sample. Knigge et al. (2006) fit the SED with both a single and a binary model, finding comparable results for the physical parameters of the BSS, although the

presence of an MS secondary improved the quality of their fit. Irrespective of the presence of a companion, the physical parameters they found from the fits point toward quite low-mass values ( $M = 0.34^{+0.15}_{-0.08} M_{\odot}$  and  $M = 0.37^{+0.15}_{-0.10} M_{\odot}$  for the single and binary models, respectively). They argue that such low-mass values can be due to systematic uncertainties in the  $\log(g)$  estimates due to uncertainties on, e.g., the cluster distance, reddening, and metallicity, or that the low  $\log(g)$  values can be due to the rapid rotation of the star. Unfortunately, without spectroscopy it is not possible to disentangle between the two scenarios. On the contrary, our mass estimate for BSS17 is  $M = 1.19^{+0.27}_{-0.22} M_{\odot}$ , larger than the TO mass and compatible with the value found for other BSSs of comparable magnitude. It is important to note that the cluster distance, reddening, and metallicity we adopted are slightly different from theirs (0.01 kpc in distance,  $-0.13$  dex in metallicity, and 0.008 in reddening), but these small differences can hardly explain the large discrepancy in the derived mass. The significant difference between these two mass values for BSS17 might be explained by the fact that we use an MCMC approach to the SED-fitting procedure, and we explicitly add a term in the  $\chi^2$  computation (see Equation (5)) to increase the sensitivity of the fit to the surface gravity.

Knigge et al. (2008) used FUV spectroscopy (obtained with the Space Telescope Imaging Spectrograph on board *HST*) to study 48 FUV-excess sources in the same FOV as this work, classifying them on the basis of their FUV-optical CMD and combining the FUV spectroscopy with UV-optical SEDs (constructed using the same photometric data set used in Knigge et al. 2006, almost coincident with ours; see the previous paragraph) to further study these sources and constrain their physical parameters. They found eight BSSs in their sample, but they analyzed in detail, i.e., obtained physical parameter estimates, only two of them (star 2 and star 999 using their nomenclature; shown as black squares in Figure 12). These two stars correspond to our BSS2 and BSS1, respectively. Regarding star 2 (BSS2), Knigge et al. (2008) detected a significant FUV excess from spectroscopy, which they associate with a WD companion. However, the photometric data can still be described by a single component since the WD emission is too blue to have a significant impact at those wavelengths. Therefore, regarding the BSS physical parameters, we can safely compare our result, obtained under the assumption of single stars (see Section 3.3), with theirs. They obtain a mass of  $1.2 M_{\odot}$  (no uncertainties reported), consistent, within the errors, with our result for BSS2 ( $M = 1.39^{+0.35}_{-0.22} M_{\odot}$ ). Regarding star 999 (BSS1), they obtain  $M = 1.9 \pm 0.4 M_{\odot}$ , fitting the broadband SED only, excluding the FUV spectrometry (see their Section 4.12 for a detailed explanation). This is also comparable to our measurement:  $M = 2.31^{+0.64}_{-0.59} M_{\odot}$ . Our BSS1 mass measurement seems to further confirm that this star, as already discussed in Knigge et al. (2008), has a mass larger than  $2M_{\text{TO}}$ . Unfortunately, both in Knigge et al. (2008) and in this work, the mass uncertainties are too large to definitively conclude that BSS1 must have had more than two progenitors.

## 5. Conclusions

We used high angular resolution *HST* ACS/HRC images to construct broadband BSS SEDs in the GC 47 Tuc. We obtained physical parameter estimates (temperature, gravity, radius, luminosity, and mass) for 22 BSSs through SED fitting,

using an MCMC approach. This is the first time that BSS masses have been obtained directly and consistently for such a large BSS sample within the same cluster.

The physical parameters we obtained are in good agreement with theoretical predictions, and in particular we find that BSSs in 47 Tuc define a mass sequence, with lower masses at fainter magnitudes and higher masses at brighter magnitudes.

We compare our SED-fit based mass measurements with estimates obtained from the BSS position in the CMD and a grid of evolutionary tracks, finding consistent results. Hence, when direct BSS mass estimates cannot be obtained, this method can be used to derive at least first-guess BSS masses.

A few BSSs in our sample have a median mass that exceeds  $2M_{\text{TO}}$ , and could therefore be the product of more than two progenitors. Our uncertainties, however, are too large to conclusively confirm these results.



We thank the anonymous referee for useful comments that contributed to improve the presentation of the paper.

Based on observations with the NASA/ESA *Hubble Space Telescope*, obtained at the Space Telescope Science Institute, which is operated by AURA, Inc., under NASA contract NAS 5-26555. This paper is part of the project COSMIC-LAB (“Globular Clusters as Cosmic Laboratories”) at the Physics and Astronomy Department of the Bologna University.

*Facility:* *HST*(ACS/HRC).

*Software:* emcee (Foreman-Mackey et al. 2013); Matplotlib (Hunter 2007); NumPy (Oliphant 2006); pysynphot (Lim et al. 2015); scipy (Jones et al. 2001).

## ORCID iDs

Silvia Raso  <https://orcid.org/0000-0003-4592-1236>  
 Cristina Pallanca  <https://orcid.org/0000-0002-7104-2107>  
 Francesco R. Ferraro  <https://orcid.org/0000-0002-2165-8528>  
 Barbara Lanzoni  <https://orcid.org/0000-0001-5613-4938>  
 Alessio Mucciarelli  <https://orcid.org/0000-0001-9158-8580>  
 Livia Origlia  <https://orcid.org/0000-0002-6040-5849>  
 Emanuele Dalessandro  <https://orcid.org/0000-0003-4237-4601>  
 Andrea Bellini  <https://orcid.org/0000-0003-3858-637X>  
 Mattia Libralato  <https://orcid.org/0000-0001-9673-7397>  
 Jay Anderson  <https://orcid.org/0000-0003-2861-3995>

## References

- Alessandrini, E., Lanzoni, B., Mocchi, P., Ciotti, L., & Ferraro, F. R. 2014, *ApJ*, 795, 169  
 Alessandrini, E., Lanzoni, B., Mocchi, P., Ferraro, F. R., & Vesperini, E. 2016, *ApJ*, 833, 252  
 Anderson, J., & King, I. R. 2004, ACS/ISR 2004-05 (Baltimore, MD: STScI) available online at <http://www.stsci.edu/hst/acs/documents/isrs>  
 Baldwin, A. T., Watkins, L. L., van der Marel, R. P., et al. 2016, *ApJ*, 827, 12  
 Baumgardt, H., & Hilker, M. 2018, *MNRAS*, 478, 1520  
 Beccari, G., Lützgendorf, N., Olczak, C., et al. 2012, *ApJ*, 754, 108  
 Beccari, G., Sollima, A., Ferraro, F. R., et al. 2011, *ApJ*, 737, 3  
 Beccari, G., Ferraro, F. R., Dalessandro, E., et al. 2019, *ApJ*, 876, 87  
 Bellini, A., Anderson, J., Bedin, L. R., et al. 2017, *ApJ*, 842, 6  
 Bellini, A., Anderson, J., van der Marel, R. P., et al. 2014, *ApJ*, 797, 115  
 Bellini, A., Libralato, M., Bedin, L. R., et al. 2018, *ApJ*, 853, 86  
 Bohlin, R. C. 2016, *AJ*, 152, 60  
 Cardelli, J. A., Clayton, G. C., & Mathis, J. S. 1989, *ApJ*, 345, 245  
 Chatterjee, S., Rasio, F. A., Sills, A., & Glebbeek, E. 2013, *ApJ*, 777, 106  
 Chen, X., & Han, Z. 2009, *MNRAS*, 395, 1822  
 Clement, C. M., Muzzin, A., Dufton, Q., et al. 2001, *AJ*, 122, 2587  
 Dalessandro, E., Cadelano, M., Vesperini, E., et al. 2018, *ApJ*, 859, 15

- Dalessandro, E., Ferraro, F. R., Massari, D., et al. 2013, *ApJ*, **778**, 135
- Dalessandro, E., Lanzoni, B., Ferraro, F. R., et al. 2008, *ApJ*, **681**, 311
- Davies, M. B., Piotto, G., & De Angeli, F. 2004, *MNRAS*, **349**, 129
- de Marchi, G., Paresce, F., & Ferraro, F. R. 1993, *ApJS*, **85**, 293
- De Marco, O., Shara, M. M., Zurek, D., et al. 2005, *ApJ*, **632**, 894
- Dotter, A., Sarajedini, A., Anderson, J., et al. 2010, *ApJ*, **708**, 698
- Edmonds, P. D., Gilliland, R. L., Guhathakurta, P., et al. 1996, *ApJ*, **468**, 241
- Ferraro, F. R., Beccari, G., Dalessandro, E., et al. 2009, *Natur*, **462**, 1028
- Ferraro, F. R., Beccari, G., & Rood, R. T. 2004, *ApJ*, **603**, 127
- Ferraro, F. R., D'Amico, N., Possenti, A., Mignani, R. P., & Paltrinieri, B. 2001, *ApJ*, **561**, 337
- Ferraro, F. R., Fusi Pecci, F., & Bellazzini, M. 1995, *A&A*, **294**, 80
- Ferraro, F. R., Fusi Pecci, F., & Buonanno, R. 1992, *MNRAS*, **256**, 376
- Ferraro, F. R., Fusi Pecci, F., & Cacciari, C. 1993, *AJ*, **106**, 2324
- Ferraro, F. R., Lanzoni, B., Dalessandro, E., et al. 2012, *Natur*, **492**, 393
- Ferraro, F. R., Lanzoni, B., Raso, S., et al. 2018, *ApJ*, **860**, 36
- Ferraro, F. R., Lapenna, E., Mucciarelli, A., et al. 2016, *ApJ*, **816**, 70
- Ferraro, F. R., Paltrinieri, B., Fusi Pecci, F., et al. 1997, *A&A*, **324**, 915
- Ferraro, F. R., Sabbi, E., Gratton, R., et al. 2006, *ApJL*, **647**, L53
- Ferraro, F. R., Sills, A., Rood, R. T., Paltrinieri, B., & Buonanno, R. 2003, *ApJ*, **588**, 464
- Fiorentino, G., Lanzoni, B., Dalessandro, E., et al. 2014, *ApJ*, **783**, 29
- Foreman-Mackey, D., Hogg, D. W., Lang, D., & Goodman, J. 2013, *PASP*, **125**, 306
- Gilliland, R. L., Bono, G., Edmonds, P. D., et al. 1998, *ApJ*, **507**, 818
- Grindlay, J. E., Heinke, C., Edmonds, P. D., & Murray, S. S. 2001, *Sci*, **292**, 2290
- Guhathakurta, P., Yanny, B., Schneider, D. P., & Bahcall, J. N. 1992, *AJ*, **104**, 1790
- Harris, W. E. 1996, *AJ*, **112**, 1487
- Hidalgo, S. L., Pietrinferni, A., Cassisi, S., et al. 2018, *ApJ*, **856**, 125
- Hills, J. G., & Day, C. A. 1976, *ApJL*, **17**, 87
- Hunter, J. D., 2007, *CSE*, **9**, 90
- Jones, E., Oliphant, E., Peterson, P., et al. 2001, SciPy: Open Source Scientific Tools for Python, <http://www.scipy.org/>
- Knigge, C., Dieball, A., Maíz Apellániz, J., et al. 2008, *ApJ*, **683**, 1006
- Knigge, C., Gilliland, R. L., Dieball, A., et al. 2006, *ApJ*, **641**, 281
- Knigge, C., Leigh, N., & Sills, A. 2009, *Natur*, **457**, 288
- Kurucz, R. L. 1993, in ASP Conf. Ser. 44, IAU Coll. 138, Peculiar versus Normal Phenomena in A-type and Related Stars, ed. M. M. Dworetzky, F. Castelli, & R. Faraggiana (San Francisco, CA: ASP), 87
- Kurucz, R. L. 2005, *MSAIS*, **8**, 14
- Lanzoni, B., Dalessandro, E., Ferraro, F. R., et al. 2007a, *ApJ*, **663**, 267
- Lanzoni, B., Ferraro, F. R., Alessandrini, E., et al. 2016, *ApJL*, **833**, L29
- Lanzoni, B., Sanna, N., Ferraro, F. R., et al. 2007b, *ApJ*, **663**, 1040
- Leigh, N., Knigge, C., Sills, A., et al. 2013, *MNRAS*, **428**, 897
- Leigh, N., Sills, A., & Knigge, C. 2007, *ApJ*, **661**, 210
- Li, C., Sun, W., Hong, J., et al. 2019, *ApJ*, **871**, 171
- Libralato, M., Bellini, A., Piotto, G., et al. 2019, *ApJ*, **873**, 109
- Libralato, M., Bellini, A., van der Marel, R. P., et al. 2018, *ApJ*, **861**, 99
- Lim, P. L., Diaz, R. I., & Laidler, V. 2015, PySynphot User's Guide (Baltimore, MD: STScI), <https://pysynphot.readthedocs.io/en/latest/>
- Mapelli, M., Sigurdsson, S., Colpi, M., et al. 2004, *ApJL*, **605**, L29
- Mapelli, M., Sigurdsson, S., Ferraro, F. R., et al. 2006, *MNRAS*, **373**, 361
- McCrea, W. H. 1964, *MNRAS*, **128**, 147
- Moretti, A., De Angeli, F., & Piotto, G. 2008, *A&A*, **483**, 183
- Oliphant, T. E. 2006, A Guide to NumPy
- Parada, J., Richer, H., Heyl, J., et al. 2016, *ApJ*, **830**, 139
- Paresce, F., Shara, M., Meylan, G., et al. 1991, *Natur*, **352**, 297
- Pietrinferni, A., Cassisi, S., Salaris, M., & Castelli, F. 2004, *ApJ*, **612**, 168
- Piotto, G., De Angeli, F., King, I. R., et al. 2004, *ApJL*, **604**, L109
- Piotto, G., Milone, A. P., Bedin, L. R., et al. 2015, *AJ*, **149**, 91
- Raso, S., Ferraro, F. R., Dalessandro, E., et al. 2017, *ApJ*, **839**, 64
- Sandage, A. R. 1953, *AJ*, **58**, 61
- Sbordone, L., Bonifacio, P., Castelli, F., & Kurucz, R. L. 2004, *MSAIS*, **5**, 93
- Shara, M. M., Saffer, R. A., & Livio, M. 1997, *ApJL*, **489**, L59
- Sills, A., Glebbeek, E., Chatterjee, S., & Rasio, F. A. 2013, *ApJ*, **777**, 105
- Simunovic, M., & Puzia, T. H. 2016, *MNRAS*, **462**, 3401
- Simunovic, M., Puzia, T. H., & Sills, A. 2014, *ApJL*, **795**, L10
- Singh, G., & Yadav, R. K. S. 2019, *MNRAS*, **482**, 4874
- Sollima, A., & Ferraro, F. R. 2019, *MNRAS*, **483**, 1523
- Sollima, A., Lanzoni, B., Beccari, G., Ferraro, F. R., & Fusi Pecci, F. 2008, *A&A*, **481**, 701
- Soto, M., Bellini, A., Anderson, J., et al. 2017, *AJ*, **153**, 19
- Watkins, L. L., van der Marel, R. P., Bellini, A., & Anderson, J. 2015, *ApJ*, **803**, 29
- Xin, Y., Ferraro, F. R., Lu, P., et al. 2015, *ApJ*, **801**, 67